



Full length article

Hydrodynamic phenomena induced by laser ablation of metal into liquid

Yu.V. Petrov^{a,c,*}, V.A. Khokhlov^a, V.V. Zhakhovsky^{b,a}, N.A. Inogamov^{a,b}^a Landau Institute for Theoretical Physics of RAS, 1-A Akademika Semenova av., Chernogolovka, Moscow Region 142432, Russia^b Dukhov Research Institute of Automatics, 22 Sushchevskaya st., Moscow 127055, Russia^c Moscow Institute of Physics and Technology, 9 Institutskii per., Dolgoprudny, Moscow Region 141700, Russia

ARTICLE INFO

Keywords:

Laser ablation in liquid
 Supercritical states
 Water adiabatic curves

ABSTRACT

Laser ablation in liquid (LAL) is a promising technique for manufacturing nanoparticles (NPs) required for modern technologies, but it is not fully understood. Deep understanding is necessary to optimize processes and decrease the high price of LAL NPs. Known studies are focused on either the bubble dynamics at late stages or ablation of material before bubble formation. Here, we consider the LAL throughout: from ablation and up to the bubble formation and inflation. Thus, we cover an extremely wide range of spatiotemporal scales, for which the roles of absorbed energy, pulse duration, and supercritical states are considered. Atom diffusion, hydrodynamic mixing due to Rayleigh-Taylor instability, and interplay between them are described.

Liquid near the contact with metal is heated by dissipation in strong shock and due to a small but finite heat conduction from hot metal after laser energy deposition. Expansion and cooling of atomically mixed liquid and metal lead to condensation of metal atoms into NPs after pressure drops below the critical pressure for metal. Development of bubble takes place during the next stages of pressure decrease below the critical parameters for liquid and below ambient pressure in liquid. Thin hot layer of liquid near the contact expands by many orders of magnitude producing the inflating bubble.

1. Introduction

Nanoparticles (NPs) are used in many important scientific and industrial applications [1, 2]. The competing chemical and laser-assisted techniques are mainly utilized for production of NPs. Chemical production is cheaper but laser fabrication is more simple, clean, and more green in an ecological sense [1, 2]. Therefore, studies directed to understand, optimize and make cheaper the production of NPs using laser ablation in liquid (LAL) are important. But today, many aspects of LAL remains unclear because it is difficult to describe theoretically the different and closely related physical processes proceeding at a logarithmically wide range of times illustrated in Fig. 1. Also the early stages, before bubble formation, remain experimentally unexplored, excepting an attempt [3] to trace the states of irradiated surface during a nanosecond laser pulse. Authors of Ref. [3] see a decrease of reflection from the gold surface in water shown in their inset in Fig. 9 (a) there.

Short lasting laser irradiation changes strongly the thermal and mechanical state of a system consisting from an absorbing target and transparent liquid or solid surrounding a target; below, we consider a gold target contacting with water or glass. Absorption of light and heating of gold through such transparent media is concentrated in an extremely thin surface disk under a focal spot; therefore, a small

amount of NPs can be produced by a single shot. Radius of the disk is defined by laser beam radius R_L (usually $R_L \sim 0.1$ mm), while its thickness equals to thickness of a heat affected zone d_T and is a fraction of micron. Further, a long multi-step process of relaxation goes after laser energy deposition. Positive and negative momenta are carried away from the surface layer by non-linear acoustic waves (shocks in water and in gold), while the heat affected zone evolves separately (from the shocks) with velocities which are small relative to the sound speed.

Today, detailed data concerning late stages beginning from $\sim 1 \mu$ s are collected [1, 2, 4]. These data include experimental measurements of the bubble radius $R(t)$ and its calculations via Rayleigh-Plesset equation [4] by determining the internal pressure $p(t)$ inside a bubble from $R(t)$ supposing that the ambient pressure used in this equation equals to the pressure inside a container with liquid before laser irradiation. We see from Fig. 1 that these data refer to the late stages of relaxation of a system after laser pulse. This is the main direction of experimental studies of LAL today.

There is rather new direction of the LAL related researches focused on mechanisms of ablation in liquid [3, 5–13], initiated at early stages of processes shown in Fig. 1. The listed papers discuss the initial ablation theoretically and by computer simulations. The paper [3] is an

* Corresponding author.

E-mail address: uvp49@mail.ru (Y.V. Petrov).

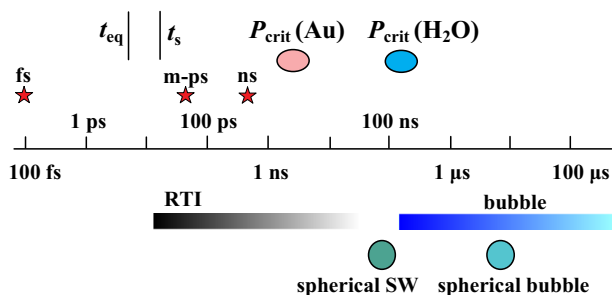


Fig. 1. The hierarchy of processes triggered by laser pulses with durations of $\tau_L = 100$ (fs), 50 ps (m-ps, multi-picosecond), and 0.5 (ns) marked by stars. Range of absorbed fluences is $F_{abs} = 0.3\text{--}1$ J/cm², laser beam radius on metal surface immersed in liquid is $R_L \sim 100$ μ m. The duration t_{eq} separates values of τ_L when the two-temperature effects at $T_e \gg T_i$ are significant in gold [11]. During the stage lasting t_{eq} the equilibration of electron and ion temperatures T_e and T_i takes place. If $\tau_L < t_s$ (stress-confinement) then the largest ratios $p/F_{abs} \sim 1/d_T$ are achieved; here p is the maximum pressure created at the end of absorption of a laser pulse. The ellipses mark stages when the contact pressure decreases below the critical pressure of gold and water. Bubble begins to form and evolves during the time range marked as “bubble.” The range “RTI” refers to the Rayleigh-Taylor instability mixing molten gold and water. Here, the beginning of the RTI range is shown for the femtosecond pulses. For longer pulses a role of RTI in mixing and production of nanoparticles decreases.

exception because the developed theory is supported with valuable experiments related to the early stages. Authors of Ref. [3] measure the reflectivity during a weak nanosecond laser pulse, at which the metal does not even melt. A theoretical part of the work [3] is based on a simple energy equation — hydrodynamical effects are neglected because of weak heating.

A temporal range covering a few nanoseconds has been studied in above cited works. But in work [11], simulations have been extended up to a sub-microsecond stages (up to 0.2 μ s). At this stage, the contact pressure p_{CB} decreases down to the critical pressure of water $p_{cr|wt} = 220$ bars, see Fig. 1.

A gold-water pair exposed to an ultrashort pulse with intensity ($I \propto \exp(-t^2/\tau_L^2)$) and pulse duration of $\tau_L = 120$ fs was considered in Ref. [5]. An aluminum-water pair was also studied in Ref. [6] for the pulse with $\tau_L = 60$ fs. There is a significant difference in results obtained in those two papers. It is caused by large difference in metal to water density ratios between gold-water and aluminum-water cases. Simulation results of the papers [5, 6] were obtained using the two-temperature 1D Lagrangian hydrodynamic code. The code is similar to our two-temperature Lagrangian code employed below. In the paper below, we compare pictures coming from hydrodynamic Lagrangian code and from molecular dynamics. This allows us to understand a role of diffusion processes absent in the Lagrangian description of motion. In the papers [5, 6, 8], authors compared ablations in vacuum and into water and investigated the qualitative difference between them connected with resistance of liquid to expansion of a hot metal.

In the paper [7], authors contrasted hydrodynamic and molecular dynamic simulations (in the problem of ablation in liquid) and report satisfactory agreement between them.

A silver-water target was considered in Refs. [8, 9]. Durations were $\tau_L = 60$ fs (the e-folding time) in Ref. [8] and $\tau_L = 6$ ps in Ref. [9]. Authors of Refs. [5, 6] used only hydrodynamic simulation, while in papers [7–9] molecular dynamics (MD) was applied. Paper [9] contains also experimental observations. Important findings have been revealed in the articles [8–11]. The role of hydrodynamic instability (Rayleigh-Taylor instability) in the formation of rather large nanoparticles was clarified. Comparing results given in works [5–11] with results presented below, we can conclude that longer durations are investigated and stronger actions are considered here. Longer durations eliminate nucleation and foaming important in the cases with ultrashort pulses.

While stronger actions lead to zeroing of the surface tension and thus enhance diffusion.

In papers [12, 13], the spatially localized along surface effect of ultrashort pulse was considered. This underlines that in the papers [5–11], spatially homogeneous cases were studied. In these papers, irradiation is homogeneous across the transverse directions (that is in the directions along the illuminated surface). In paper [12], gold expands in vacuum while in Ref. [13] gold expands in water. Differences between the results below in the text and in the papers [12, 13] are: (i) tight focusing is considered (as was said, illumination is inhomogeneous along the surface); (ii) 2D situation is analyzed — cylindrical lens creates an illuminated narrow straight line on a surface.

We consider systems made from the pairs gold-water (Au-wt) and gold-silica (Au-gl, glass). The critical parameters are: $T = 7.8$ K, $\rho = 5.3$ g/cm³, $p = 5300$ bar for gold [14–18] (see also Fig. 4 in Ref. [11] where saturation pressure of gold vapor is plotted) and $T = 647$ K, $\rho = 0.3068$ g/cm³, $p = 220$ bar for water. The signs (marking achievement of critical parameters) at the logarithmic axis of time in Fig. 1 corresponds to simulations presented in Ref. [11] where duration of a laser pulse was $\tau_L = 0.1$ ps. In the present paper, we use data from Ref. [11] together with new information obtained in described below simulations corresponding to pulse durations 50 ps and 0.5 ns. These durations are marked by the red stars in Fig. 1. They are significantly longer than previously studied.

Adiabatic expansion toward the critical pressure of water in the near contact boundary (CB) layer at sub-microsecond stage was calculated in Ref. [11]. At this stage, the shock in water passes a distance of the order of a radius of an illuminated spot (~ 100 μ m). At the later stage, the shock transits from the quasi-plane spatial shape to the quasi-spherical shape. This transition for the spots ~ 100 μ m is marked in Fig. 1 as “spherical SW”. The heated water layer mixed with gold in the atomic and cluster states expands much more slowly relative to the shock. Thus, the system simulated in Ref. [11] did not reach the stage of bubble formation, which is marked in Fig. 1 as “spherical bubble”.

In order to consider not only formation of a bubble but to analyze late stages of bubble expansion, here we construct one-phase (gaseous) and two-phase (liquid-vapor) adiabatic curves of water. These adiabatic curves start from a Hugoniot adiabatic curve in water or from a heated state of water. At late stages, the volume of gaseous water filling a bubble increases many orders of magnitude relative to initial volume of a heated contact water layer. Thus, we make a bridge between the early (ablation) stages and the late (oscillations of a bubble) stages, which bridges a gap between two kinds of LAL studies.

As of now, there are objective experimental and theoretical difficulties in observing and understanding the early stages, unlike the late stages which are explored well. Current understanding of LAL has a gap between the early and late stages. Our goal in this work is to extend simulations as long in time as possible and predict water states at the late stages.

We present studies of LAL with the usage of both hydrodynamic (HD) modeling and molecular dynamics (MD) simulations. Such combined approach allows for metal-liquid diffusion and mixed Lagrangian cells (where both components are presented in a cell) which are not allowed in the Lagrangian HD code alone [5, 6, 11]. New effect discussed below is connected with the higher radiative laser fluxes than those used in MD simulations published before, which is significant because the near contact temperatures are higher enough to eliminate the surface tension thus opening a way for intensive diffusive mixing. Such supercritical states at higher laser fluences were observed also in Ref. [6]. Here, the much longer pulse durations (than considered before) are investigated in order to fall within the nanosecond pulses used in practical applications.

The longer durations together with active diffusion significantly suppresses a rate of development of the Rayleigh-Taylor instability. By contrast, this instability is well developed for the ultrashort pulses, which results in generation of relatively large nanoparticles [8, 9, 11],

while diffusion and condensation produce smaller ones.

The paper is structured as follows. The heating and acoustic processes are discussed in Section 2 where the laser pulses significantly longer than the acoustic time $t_s = d_T/c_s$ defined as a sound traveling time of heated layer with thickness d_T are considered. We compare those long pulses with the ultrashort ones $t_s \ll \tau_L$ considered previously in Refs. [5–13]. There are four striking consequences following from these comparisons.

First, nucleation and foaming take place even for intermediate durations $\tau_L \sim t_s$ when stress confinement [19] is rather weak; it is well known [19] that nucleation exists above a threshold for thermo-mechanical ablation by the ultrashort pulses with $\tau_L \ll t_s$. Second, it is important that the nucleation disappears for nanosecond pulses. The internal structures created in liquid during expansion are different in the cases with and without nucleation. Third, even slow heating by a nanosecond pulse produces dynamically significant acoustic irradiation from the heated layer. And fourth, the acoustic wave created by a long pulse has a spatial profile at $t \sim \tau_L$ which differs qualitatively from the triangular shape typical for ultrashort pulses. This wave becomes triangular only later in time.

Separation of acoustic waves moving in the bulk of metal and in the bulk of liquid is discussed in Section 3. Evolution of the slowly moving (relative to sound speed) layers near a contact boundary is described in Section 3. Transition to supercritical states is presented in Section 4. Situation is similar to that considered in Ref. [6]. But here, MD is used thus the diffusion processes are included. Expansion of a heated layer of water to very small densities is studied in Section 5.

2. Heating regimes during laser pulse

There is an expressed time t_s separating the ablation regimes on short/fast one with $\tau_L \ll t_s$ and to long/slow (subsonic) one with $\tau_L \gg t_s$ according to the pulse duration τ_L . This time $t_s = d_T/c_s$ is defined by competition between acoustic phenomena and heating (rate and duration of heating), see Fig. 1. Here, c_s is sound velocity in an absorber. Typically, the sound speed in solid at room temperature before a laser action is taken for estimates; e.g., for gold $c_s = 3.1$ km/s. It is also reasonable to set d_T to a thickness of a heat affected zone (HAZ) achieved at the time $t = t_s$.

There is a subregime in the short/fast regimes, at which the duration τ_L of used ultrashort laser pulse (UsLP) is shorter than an equilibration time t_{eq} mentioned in Fig. 1. Often such pulses are classified as femtosecond (fs), but in fact such pulses have sub-picosecond durations. Their durations are shorter than the equilibration time t_{eq} of the two-temperature (2T) stage, at which electrons absorbing the laser energy are much hotter than ions $T_e \gg T_i$. Main physical features of 2T stage were revealed in the pioneer work [20]. Two important characteristics are the electron-ion coupling parameter α and the great electron heat conduction κ during the 2T stage [21, 22], because the semi-degenerate electrons with rather small heat capacity c are partially decoupled from a classical ion subsystem with large heat capacity [23], thus the electron thermal diffusion coefficient $\chi = \kappa/c$ is enlarged by 10–100 times [21, 22, 24] above its usual value ~ 1 cm²/s corresponding to the one-temperature (1T) conditions.

Fast electron thermal conduction in the 2T stage looks unusual in comparison with that in the 1T stage. It carries out the thermal energy accumulated in electrons from a skin layer [25] with a supersonic speed [26]. Supersonic expansion of such electron thermal wave continues during the 2T stage [21, 22, 24], therefore the equilibration time t_{eq} works as an effective heating duration exceeding the UsLP duration. The thermal wave is fast thanks to high electron thermal diffusion coefficient χ . Supersonic expansion of heat means that during its existence the spatial expansion of matter is delayed (relative to propagation of heat), that is density remains approximately equal to its values before the laser action (isochoric regime); except the thin layer near the contact boundary (CB). Thus, for UsLP a heat affected zone is mainly

created during the 2T stage: $d_T = 2\sqrt{\chi t_{eq}}$,

$$d_T(\chi_{1T} = 1 \text{ cm}^2/\text{s}, t_{eq} = 1 \text{ ps}) = 20 \text{ nm}, \quad d_T(\chi_{2T} = 20 \text{ cm}^2/\text{s}, t_{eq} = 7 \text{ ps}) = 240 \text{ nm}.$$

These estimates emphasize the difference between 1T diffusion and enhanced one, and the role of the prolonged 2T relaxation for long t_{eq} . For gold, the last values (in the above line for d_T) of χ_{2T} (enhanced electron diffusion) and t_{eq} (extremely delayed relaxation thanks to a heavy ion) are typical [21, 22, 25, 27]. Position of the mark t_{eq} in Fig. 1 corresponds to the case of gold. We say “extremely delayed” in the meaning of comparison of gold (Au) with poorly conducting metals like Ni, Pt, or Ta where diffusion is weaker while an electron-ion coupling is stronger [28].

The short pulses with $\tau_L \ll t_s$ leads to the stress confinement conditions while the long pulses with $\tau_L \gg t_s$ produce the heat confinement regimes [19]. After formation of heat affected zone (HAZ) by a short pulse, the acoustic decay of the stress confinement proceeds in HAZ during t_s . While the HAZ emits acoustic waves outward the heat remains in the HAZ. In the next section, we will consider separation of acoustic and entropy-vortical hydrodynamics modes and their existence long after the separation that is at the stages $t \gg t_s$, while the acoustic near-field region $t \sim t_s$ is discussed here. In one-dimensional geometry, the vortex is excluded therefore the only acoustic and motionless entropy modes are present in adiabatic (without thermal conductivity) hydrodynamics. If we take into account the thermal conduction, then the entropy s will spread from material particles.

In the long-pulse regime with $\tau_L \gg t_s$, the generated pressures are relatively low, and separation in time to the near-field temporal region and to the far-field temporal region loses its meaning, because the heated region (skin and conduction layer) continuously emits outward the weak acoustic signals during such a long pulse. After the laser pulse, the acoustic emission is completed and two opposite trains of acoustic waves propagate toward the bulk gold and water.

Thermal expansion of material produces mass motion in both cases with $\tau_L \ll t_s$ and $\tau_L \gg t_s$. The displacement of a contact boundary (CB) Δx is proportional to a coefficient of thermal expansion $\beta \sim 0.1/T_{cr}$, increase of temperature T , and length d_T of the HAZ: $\Delta x \sim (\rho_0/\rho_{HAZ} - 1)d_T$, where β is a value of the thermal expansion coefficient at the room temperature, ρ_0 and ρ_{HAZ} are initial density and density after thermal expansion. Density ρ_{HAZ} is twice and more times less than ρ_0 in the considered here conditions. Thus the displacement Δx is a fraction of 1 μm typically because d_T is one or few hundreds of nanometers.

Resuming the last two paragraphs, we can say that a shock generated by a short laser pulse have a shorter shock-affected layer behind the shock front (with thickness $\sim d_T$) and have larger pressure than a shock generated by a long pulse with $\tau_L \gg t_s$. While the evolutions of the near CB hot layers after finishing of a pulse differ less; these layers are called also the layers connected to the entropy or advection mode.

Below, the full hydrodynamic simulation, including heat conductivities of gold and water, and motionless modeling of thermal problem of laser absorption and heat spreading are compared. Sometimes, authors limit themselves with this motionless modeling assuming that material motion is very slow and therefore insignificant for a long laser pulse. Thus, such approach neglects density variations. But as was said before, the thermal expansion leads to a strong decrease of density in both cases (fast and slow) if absorbed energy is large enough. For a long pulse, these changes develop slowly but at the end of pulse they are of the same order as for a short pulse.

For better understanding and to emphasize an importance of pulse duration, we performed simulations related to the edges of the fast-slow range of durations and to the middle of this range. For gold, the d_T is about 150 nm for fast and slow regimes, which gives the acoustic time $t_s \sim 50$ ps shown in Fig. 1. For τ_L equal to 0.1, 50, and 500 ps, the ratios τ_L/t_s are 0.002, 1, and 10, respectively for the fast, intermediate, and slow regimes of laser action, which are specified by the three red stars in Fig. 1. The set of simulations covering the fast/slow ranges is described in Table 1. They are simulated by 2T-HD, 1T-HD, 1T-without

Table 1

Eight simulations with different pulse durations. Here, pairs Au-water or Au-glass are presented. Entire simulation time is given in the column t_{end} .

#	τ_L (ps)	F_{abs} (mJ/cm ²)	Medium	t_{end} (ns)	Code
0 [11]	0.1	400	Water	200	2T-HD
I	50	338	Glass	0.5	1T-HD
II	50	559	Glass	0.5	1T-HD
III	50	897	Glass	0.5	1T-HD
IV	50	400	Water	1	1T-HD
V	500	900	Water	1	1T-HD
VI	500	900	Water	10	1T-without HD
VII [11]	1	700	Water	1	MD
VIII, wide	1	2500	Water	2	MD
IX, narrow	1	2500	Water	10	MD

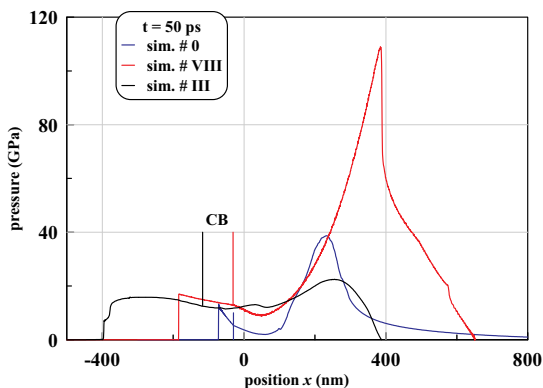


Fig. 2. Profiles of total pressure for simulations listed in Table 1 are shown for times when the 2T effects become small. The blue, red, and black straight lines mark the current positions of CB in the corresponding simulations #0, #VIII, and #III. For the fast actions (#0, #VIII) there are (i) large differences in pressure inside the dense metal and light dielectric, (ii) early formation of shock in dielectric, and (iii) a triangular shape of a shock wave in dielectric. While for the long actions (# III) there are (i) pressures in dielectric and metal differ weakly, (ii) shock in dielectric is formed later, where a some smeared acoustic perturbation is formed at the initial stage, and (iii) the shape of such acoustic perturbation differs much from a triangular shape.

HD, and MD codes; here HD and MD stand for hydrodynamics and molecular dynamics; “without HD” means that only thermal equation is solved in the conditions of the isochoric heat absorption and transfer.

Figs. 2 and 3 present profiles at $t = t_s$, when the acoustic and entropy modes begin to decouple. Simulations #0 and # VIII correspond to the ultrashort laser pulses. But the absorbed energy in case #VIII, is approximately five times larger than in the case #0. Thicknesses of the

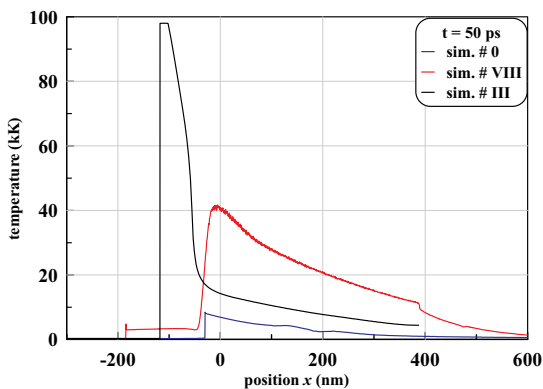


Fig. 3. Temperature profiles for the simulations #0, #III, and #VIII listed in Table 1. In the case #0, the ion temperature T_i profile is given. The 2T effects become weak at the shown time.

gold films are 1700 nm (#0), 550 nm (#VIII), and 370 nm (#III).

For the ultrashort laser pulses and a thick (bulk) gold target, there is a rather strong difference between pressures p in gold and that in transparent dielectric, see Fig. 2; here, we compare pressure inside the bulk gold and in a shock front in dielectric; pressures in gold and dielectric are equal at the CB. Large pressure difference is explained by a decay of the pressure jump linked with the CB [11]. Pressures in the contacting materials after decay of a jump (outside the vicinity of the CB) depend on their acoustic impedances, see explanations in Ref. [11]. In the intermediate case $\tau_L \sim t_s$ and for a long pulse $\tau_L \gg t_s$, the pressure profiles cannot be explained using the simple model with decay of a pressure jump.

The shock in transparent liquid or solid dielectrics appears almost immediately with the ultrashort laser pulse, because such pulse is sharp and has absorbed energy F_{abs} large enough to produce NPs. As a result, the corresponding generated pressures are larger than the bulk modulus of those materials which means that the shocks in the considered dielectrics are strong in such conditions. At the same time, the compression wave in gold is weakly or moderately non-linear because pressures in gold are less than the bulk modulus of 180 GPa of gold. Therefore, some time is required before the compression wave in gold will overturn with formation of a shock [29, 30]. While for a long pulse, the pressures are smaller and increase slowly during a pulse. Hence, longer time is necessary to wait for their overturning.

In gold near the CB, the temperature increases and density decrease with increasing F_{abs} . Also, intensity $I_{inc} = F_{abs}/A/\tau_L$ of incident light increases; here $A = 1 - R$ is an absorption coefficient. There is a transition to plasma corona like expansion into vacuum at high intensities I_{abs} . In a plasma corona, the density drops to values much lower than the solid state density (orders of magnitude lower). Light absorption takes place at plasma critical density ρ_{pl} where frequency of laser light equals to local plasma frequency of a rarefied ionized metal. In the case with transparent dielectrics, two limitations appear at the way to corona like expansion.

First, the metal target cannot be irradiated with a pulse of very high intensity because the optical breakdown will shadow the target, perhaps such effect responds for decreasing reflectivity observed in Ref. [3] during a laser pulse. Second, the density of expanding metal cannot drop below the plasma critical density ρ_{pl} during a nanosecond pulse due to confinement by dense dielectric, as opposed to expansion to vacuum. For reference, $\rho_{pl} \sim 0.1 \text{ g/cm}^3$ for optical lasers and ionization of one electron per atom in gold. We see examples with high temperatures (and hence low densities) in Fig. 3. But still, they are far from the plasma critical density. Corresponding absorbed fluences in our simulations listed in Table 1 relate to the edge of the largest fluences used in typical experiments [1, 2].

3. Separation of acoustic zones and hot advection layer

Let's consider the times $t \gg t_s$ that comes after decoupling of acoustic and entropy modes in a HAZ, which are clearly seen in the short/fast regimes $\tau_L \ll t_s$ while for a long pulse they begin later $t \gg \tau_L > t_s$. Fig. 4 obtained for the ratio $t/t_s = 20$, $t = 1 \text{ ns}$, $t_s \sim 50 \text{ ps}$, and $\tau_L = 50 \text{ ps}$ demonstrates the typical situation that happened at those times. Later time, the situation doesn't change in the sense that the triangular SWs and the advection layer are far away and independent from each other. For the later times, it is difficult to plot the SWs and advection layer together because their thicknesses become too small relative to the distances separating them.

Fig. 4 proves that heat is kept inside the entropy mode localized in a skin layer, where the primary absorption of laser energy happens. For optical lasers, the skin is a thin (10–20 nm thick) layer at the CB. Heat conductivity smears thermal energy distribution spreading heat from a skin. Spreading is very subsonic thus a clearly seen thin front of subsonic melting appears in Fig. 4, where it corresponds to a density jump marked as “melt”. Let's mention here that melting at the 2T stage

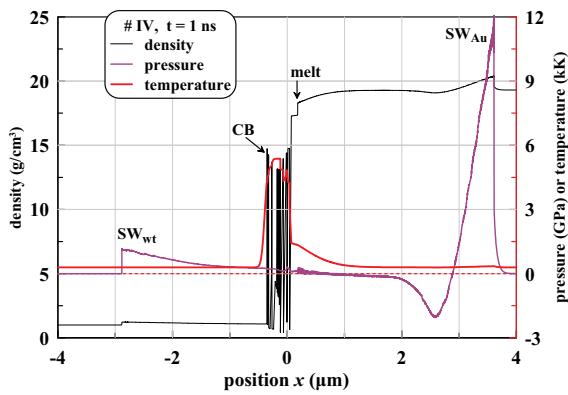


Fig. 4. Spatial separation of the triangular shock waves (SWs) and the entropy mode. The heated layer locates near the contact boundary (CB). Low heating by SW in water is invisible in the used temperature scale. Thermal energy remains concentrated inside the entropy mode called also advection layer because it doesn't move relative material particles with speed of sound as an acoustic mode but stays frozen into matter and moves (that is advected) together with matter. Entropy mode locates in a skin-layer, where it was introduced into matter, and it spreads out from the skin due to thermal conduction. Conductivity of gold is two-orders of magnitudes higher than that in water, therefore the thermal spread into the gold side is much wider. At the shown time, the “melt” marks not a melting front but a recrystallization front moving to the left with speed of 180 m/s, see details in the text.

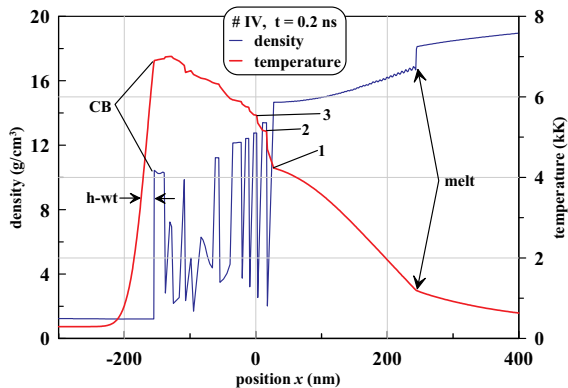


Fig. 5. Density and temperature profiles. Heat conduction spreads thermal energy from a HAZ to the right causing melting of gold. The note “melt” marks a current position of the melting front resulting in density decrease. Because the thermal conductivity drops approximately 2.5 times after melting the temperature gradient is larger in the liquid gold. The melting front moves with speed of +350 m/s relative to material at the shown time. Mass velocities of liquid and solid phases at the melting front are –100 and –70 m/s toward the water, respectively.

generated by the UsLP is smeared covering a significant part of a supersonic thermal wave [31] — such type of melting is called homogeneous nucleation of liquid phase happened at $T_{melt}(p)$, $\rho \approx \rho_0$. Thus, the Stefan problem approximation of melting/freezing isn't applicable at the 2T stage, while it is applicable in the situations shown in Figs. 4 and 5. In these figures, the melting/freezing front, first, is associated with a density jump corresponding to the edges of the triple point at the $\rho - T$ or $\rho - p$ phase planes. Second, temperature at the jump equals to the temperature of the triple point, which is 1337 K for gold.

Our approach utilizes hydrodynamic equations together with energy balance and heat conduction coupled with equation of state (EoS) of real material. Thus, an extra consideration of the Stefan problem is not required here because the melting and crystallization processes are implicitly included in the EoS describing the phase transitions (melting and evaporation) with taking into account the heats of fusion and

evaporation. Moreover, the Stefan problem is usually solved ignoring material motion produced by density change at the melting front, but such effect is observed in our simulations, see the caption to Fig. 5 where difference in hydrodynamic velocities in the solid and liquid phases at the melting front is discussed.

We follow carefully the thermal evolution of the entropy mode at a stage beginning from 150 ps before the time 1 ns shown in Fig. 4. Initially, the 1T-HD simulations (with and without HD) start at a time equal to $-3\tau_L$, see an example with $t = 200$ ps presented in Fig. 5. This figure describes the situation with heating and formation of foam in more details relative to Fig. 4 showing a global structure. What keeps the high temperature inside the foam?

In simulation #IV (see Table 1 where the simulations are listed), temperatures inside the entropy mode were 9.4 kK at the end ($t = 50$ ps) of absorption of the $\tau_L = 50$ ps pulse. The full width at half maximum of the temperature profile $T(x, t = 50$ ps) is 180 nm. After that, temperature gradually decreases mainly due to heat conduction into bulk gold and adiabatic cooling. Heat conduction in water is included but it is small and weakly affects the temperature distribution in metal at the rather early stages.

Nucleation of future foam begins at $t \approx 80$ ps in simulation #IV. During few tens of picoseconds, the nucleation process spreads in the gold layer of $d \approx 90$ nm which is marked as “foam” in Fig. 6. Mass thickness of the foamy layer is $\sigma = d \rho_0 = 1.7 \cdot 10^{-4}$ g/cm², where $\rho_0 = 19.3$ g/cm³ is the initial density of gold. After that, the column mass σ doesn't change with time in contrast to the geometrical thickness d_{geom} of the foamy layer increasing with time. The d_{geom} is 430 nm at the time $t = 1$ ns shown in Fig. 4.

Foaming decreases heavily the thermal conduction in gold, which preserves the temperature of entropy mode shown in Fig. 4. In 1D geometry used in our hydrodynamic codes, the foamy zone consists from alternating liquid (the numerals 2 and 3 in Fig. 5 mark two of these liquid layers) and vapor layers (the numerals 1–2 in Fig. 5 mark the first vapor gap from the gold side). Specifically, the vapor layers conduct heat weakly. As a result, the temperature profile in the foamy zone is composed from the ladder of steps labelled by the numerals 1, 2, 3,... in Fig. 5. Those steps have approximately uniform temperature distributions inside the liquid layers, but temperatures rise steeply in vapor layers between neighboring liquid layers. In real 3D geometry, the foamy zone contains a mixture of membranes, droplets, and vapor [11, 32–34]. Because vapor surrounding the droplets is weakly conductive, the droplets lose their thermal contact with bulk gold and hence remain hot. But some contacts are comprised of membranes attaching to the crater bottom.

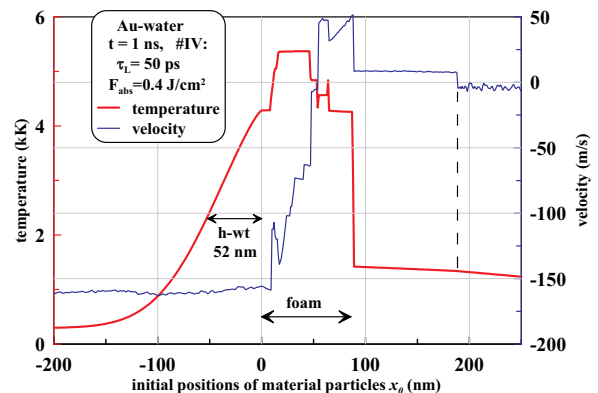


Fig. 6. Internal structure nearby the contact boundary, marked as “CB” in Fig. 4, between gold on the right and water on the left. At the Lagrangian axis x_0 the position of the CB is motionless and equal to $x_0 = 0$. The entropy/advection mode consists from foamy layer “foam” and the left warm part of the continuous gold. It is reasonable to add the heated layer of water “h-wt” to this mode. This layer begins at the hot CB, see also Fig. 5.

Continuous gold adheres to the foam independently from the foam cooling. The contact between the foam and continuous gold is denoted by the numeral 1 as shown in Fig. 5. There is a large temperature jump at this point, which is enhanced with time (Comp. Fig. 5 from one side and Figs. 4, 6 from the other side). Such enhancement takes place due to low conductance of isolating vapor layer and fast cooling by heat transfer into bulk of continuous gold.

The melting/recrystallization front moves in gold to the right until the internal energy is enough at the left side. The melting front velocity at $t = 0.2$ ns is given in Fig. 5. But later, the thermal reservoir at the left side is exhausted and the melting changes to the recrystallization [31, 35]. Then, the front is directed to the left side. Fig. 4 shows a recrystallization front moving to the left with velocity $v_{recr} = -180$ m/s with reference to material. Soon at $\approx t = 2-3$ ns, whole continuous gold adhering to the foam becomes solid.

Typically, the maximum velocity of recrystallization is about 100 m/s in gold. Rate of diffusion of atoms in a liquid phase limits the recrystallization velocity v_{recr} [32, 33, 36], but our hydrodynamic simulations gives a larger velocity corresponding to formal application of the Fourier's law for thermal conductivity connecting ∇T and v_{recr} [31, 35]. Sure, the real states produced by a sub-nanosecond pulse are not equilibrium ones as assumed in the Fourier's law, but still the velocities v_{recr} are comparable. From kinetic description, it follows that: (i) a liquid phase is overcooled below the triple point temperature; (ii) there is smearing of recrystallization front due to nucleation of nanocrystals in the bulk of liquid ahead of the front; and (iii) solidified gold transits into a polycrystalline state with extremely small sizes (few nanometers) of the crystalline grains [8, 19, 32, 33, 36–41].

The foamy part of the entropy/advection mode covers the column mass $0 < x_0 < 90$ nm in Fig. 6, where the coordinate x_0 is a Lagrangian coordinate. The Lagrangian coordinate is defined by initial (before laser pulse) position of a material particle at the axis x perpendicular to the surface. Velocities inside the thin liquid layers oscillate due to slowly decaying acoustic modes coupled to the liquid layers in the foamy zone. The foamy zone or foamy layer consists from the sequence of the thin liquid layers separated by the “vapor” intervals. Liquid layers are dense and keep their densities in time, while density at the “vapor” intervals gradually decreases with time. Spatial expansion of the foamy layer is provided namely by expansion of the “vapor” intervals. Therefore, there are significant gradients of longitudinal velocity inside the “vapor” intervals while inside the liquid layers the absolute values of this gradient is small. The acoustic modes (running, reflecting, and decaying slowly inside the liquid layers) are generated by the ruptures of continuous molten gold.

The end position of nucleation “wave” propagating into gold depends on local competition between the local tensile stress and strength of gold. The tensile stress is created due to expansion into material with a lower acoustic impedance, here in water. Tensile strength of gold depends on phase state and decreases with increasing temperature. Therefore, the nucleation wave should stop at some depth which determines the thickness of foamy zone along material axis x_0 shown in Fig. 6, where the thickness is underlined by the arrow “foam”.

Solidification is accompanied by contraction of gold. This causes appearance of mass flux of liquid to the solidification front with velocity of ≈ 20 m/s, which leads to the velocity jump shown in Fig. 6. Position of the jump is marked by dashed vertical straight line. Solidification/recrystallization front is shown by intersection of the dashed line with a temperature profile in Fig. 6. Solidification gives back the heat of fusion, which slows down the rate of temperature decrease in the entropy/advection mode outside the foamy zone.

All simulations #IV–#VIII listed in Table 1 include the heat conductivity κ_{wt} of water. Because for #IV–#VI, the $\kappa_{wt} = 0.6$ W/K/m and heat capacity 4.2 J/K/g are taken, then the thermal diffusivity is $\chi = 1.4 \cdot 10^{-3}$ cm²/s for water with normal density. In MD simulations #VII and #VIII, the heat conductivity is defined by the used interatomic potential for water molecules treated as point atoms, description of

which needs a separate discussion. Water is heated through the CB from the hot gold. Using MD simulations, we estimate the Kapitza resistance for water-gold interface. This type of resistance is linked to difference of mass of atoms and atomic character of heat conduction in water. MD simulations show that the temperature jump due to Kapitza resistance is of the order of 100 K, which is small relative to multi kilo Kelvin temperatures of gold in our conditions. Detailed discussion of this effect is beyond the scope of this article.

Because the temperature of water near the CB is high, a hot thin layer of water marked as “h-wt” appears, see Figs. 5 and 6. The line “h-wt” is plotted at the half maximum of a temperature profile (initial temperature 300 K is subtracted). The estimate $2\sqrt{\chi t}$ gives 25 nm for $\chi = 1.4 \cdot 10^{-3}$ cm²/s and $t = 1$ ns. This is approximately a half of thickness “h-wt” shown in Fig. 6.

Formation of foam in gold decreases the heat conductivity to the bulk of gold target, which leads to slower cooling of foam and gaseous gold. Thus, the supercritical gaseous gold discussed in the next section can remain hot for a long time.

4. Supercritical states

4.1. Early stage

Thermal spreading of absorbed energy F_{abs} from a skin layer during the two-temperature stage $t < t_{eq}$ creates the heat affected zone (HAZ). It is clear that the HAZ thickness $d_T \approx 150-200$ nm is the same for gold in vacuum and under water at a given F_{abs} . Distribution of absorbed energy of the order of one to few J/cm² in the HAZ transfers gold into a hot dense state above the critical point. Fig. 7 presents early structures formed in a gold-water system shortly after a powerful ultrashort laser pulse (MD simulation #IX, see Table 1). Below, we discuss how those structures change gradually at later times.

Further in time at the acoustic time scale $t_s > t_{eq}$, the HAZ acoustically decays into the entropy mode and into two acoustic compression waves running one to the contact with water and the other one to the side of bulk gold; let's call the last wave CW-bulk — compression wave propagating to the bulk side. The acoustic CW compression wave running to the contact reflects from the contact as a rarefaction wave (RfW) running behind the CW-bulk. Reflection and the reflected wave RfW depends on mechanical properties of water — the acoustic impedance of water in linear acoustics.

The time $t = 48$ ps shown in Fig. 7 approximately corresponds to the scale $t_s \approx 50-70$ ps in gold. For high energy deposition, the CW-bulk quickly overturns forming a shock wave SW_{gold} . The RfW denoted as “unloading” (into water) in Fig. 7 sits at the front of the SW_{gold} . The sitting or “attaching” to the front means that the SW_{gold} separates the flow to two regions: first at the right side relative to the SW doesn't

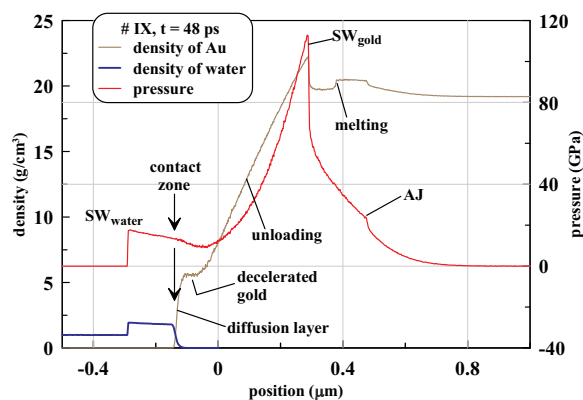


Fig. 7. Density and pressure profiles obtained from MD simulation with absorbed fluence of 2.5 J/cm². Structure of flow is shown at the stage when a compression wave leaves the heat affected zone, see details in the text.

know about expansion into water, second at the left side depends on mechanical properties of material surrounding a gold target, i.e. it knows about water. The right region is identical to that formed in vacuum surrounding at the same F_{abs} .

Fig. 7 shows an acoustic jump (AJ) formed when the CW-bulk transits through the melting front. At the two-temperature state and large overheating above the melting temperature $T_{melt}(p)$, the melting zone propagates supersonically; this regime is also called quasi-homogeneous melting. A pressure profile created during the two-temperature stage with $t_{eq} \ll t_s$ thanks to approximately isochoric heating, has a more steep spatial piece of the profile in the place where the melting zone locates at the transition stage from the two-temperature to one-temperature regime. Derivative $\partial p/\partial x$ is steeper at this piece because the pressure rise with temperature $\partial p/\partial T|_p$ as a function of temperature at fixed p is large at the isochoric melting interval between solidus and liquidus. At the acoustic stage, this steep piece propagates along the sonic characteristics with sound speed, i.e. the two-temperature supersonic melting is imprinted into profile of the CW-bulk. Because the speed of sound depends on pressure, this steep piece becomes steeper gradually which results in formation of the AJ shown in Fig. 7.

In Fig. 7, the melting front is marked. At the stage shown, the front propagates to the right side increasing mass thickness of molten gold. The SW_{gold} and RfW in Fig. 7 were discussed above.

Gold at the plateau at the left side of the RfW near the contact with water moves approximately with the same velocity as the contact. This is typical for solutions with acoustic decay of a jump separating two homogeneous semi-spaces. A high pressure semi-space produces a shock in a low pressure semi-space, while a rarefaction wave propagates into the high pressure semi-space. There is a region of homogeneous flow (a plateau) covering a shock compressed layer and a piece of matter belonging to the initially high pressure semi-space. Stretching of matter is low at the plateau while it is finite in the RfW .

In our case, the jump between semi-spaces separates the initially homogeneous semi-space (water) and a high pressure region of finite thickness d_r . Therefore, situation changes relative to classical decay of two homogeneous semi-spaces as RfW runs out from the region d_r . Contact begins to decelerate, density outside the plateau decreases down to density at the plateau. Deceleration of the contact causes deceleration of the SW_{water} in Fig. 7. In addition, triangular shape of a water shock and the profile behind it gradually forms.

Densities of gold and water are shown separately in Fig. 7. We see that in the diffusion zone, the concentrations of mixed gold and water gradually changes from 100% to 0. Diffusion smears contact into a mixing zone (arrow “contact” in Fig. 7).

Fig. 8 shows how the spatial structure demonstrated in Fig. 7 is represented on the phase diagram of gold. Phase coexistence curve (binodal), solidus, and liquidus of gold are taken from Refs. [14–18].

All typical points of the structure are given in Fig. 8. The AJ is in a solid state below the melting region. Melting happens slightly higher than the melting region because the dependence $T_{melt}(p)$ from our embedded atom method (EAM) potential is slightly different from the melting line taken from the equation of state [14–18]. SW in gold and RfW follow above the mark “melting” in Fig. 8. Pay attention to the projection of the plateau “decelerated gold” in Figs. 7 to 8, it corresponds the most hot region.

The diffusion zone follows after the plateau in direction from deep gold to water. In this zone, the temperature of gold falls down to temperature of water outside the mixed zone, while the concentration of gold atoms presented by the orange rhombuses in Fig. 8 decreases to zero. The chain of blue circles presenting water with near zero density corresponds to the low concentration of water deep in gold, see the blue curve in Fig. 7 prolonged to the right side from the mixing layer. The chain of the blue circles starting in the left up corner in Fig. 8 and going down increasing density and decreasing temperature relates to water in the mixing zone. At the left down corner, the blue circles correspond to bulk water, shock in water, and shock compressed layer of water.

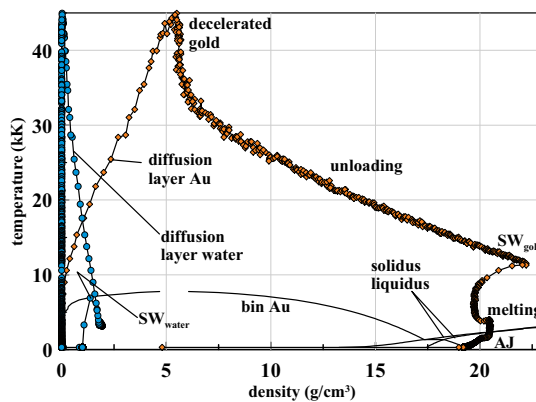


Fig. 8. Binodal curve (bin Au) and the melting region between solidus and liquidus are shown together with the structure of flow presented in Fig. 7. $F_{abs} = 2.5 \text{ J/cm}^2$ transfers gold into the supercritical states. The orange rhombuses correspond to gold, the blue circles correspond to water.

4.2. Times around nanosecond

The middle stage with structure of flow at the times near 1 ns is shown in Figs. 9–11. Because the shock in water is going far away from the contact zone, it does not affect the current dynamics nearby the contact, and thus isn't shown in our figures. A thick layer of foam in Fig. 9 separates the contact from gradually solidifying continuous bulk gold. The melting/solidification process in continuous gold located at the bottom edge of foam was illustrated in Figs. 4–6.

States of matter in foam are clearly seen in Figs. 9 and 11. This is the two-phase liquid-vapor mixture occupying the both branches of the binodal curve: one component of the mixture is located on the boiling curve corresponding to liquid phase while the other one is on the condensation curve presenting saturated vapor. Temperature of mixture decreases slowly and gradually to the right side in Fig. 9. The bottom edge of mixture is adjoint to continuous gold while the top edge transfers gradually to an atmosphere, see Fig. 9.

We call as “atmosphere” the layer between the contact and foam because this layer is in quasi-hydrostatic equilibrium with the contact. This means that the layer decelerates approximately as the contact. Spatial gradient of velocity is decreased in the atmosphere relative to

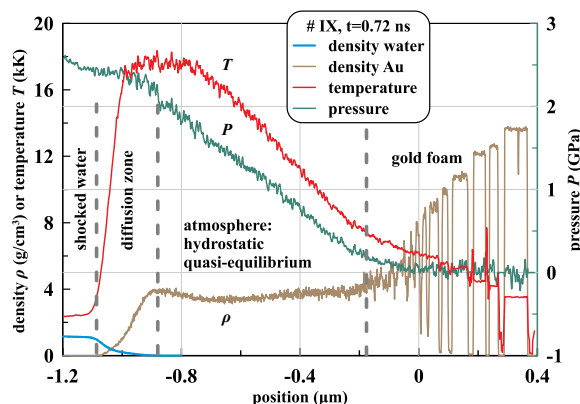


Fig. 9. Temperature, pressure and density profiles for gold in water. From right to left the structure of flow consists of foam, atmosphere, diffusion zone, and shock compressed water. Gradient of pressure in atmosphere is balanced by effective weight in the non-inertial frame attached to the contact. Density in atmosphere varies weakly due to rise of temperature of gold in direction to contact. It is interesting that molecular heat conduction in water cannot overcome heating of water connected with atomic diffusion of gold. Outside the diffusion layer water is heated thanks to thermal dissipation behind a strong shock in water.

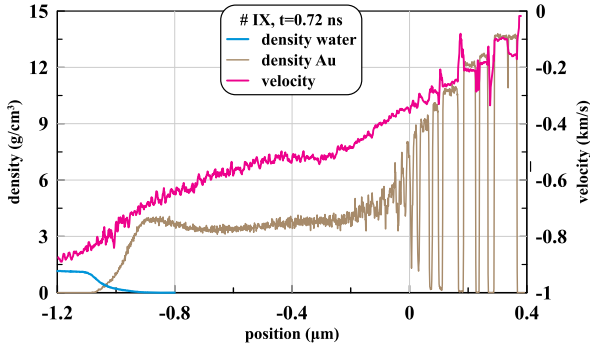


Fig. 10. Velocity and density profiles for gold in water. Gradient of velocity is less in the atmosphere, which means that material in atmosphere moves approximately with velocity determined by the gold/water contact.

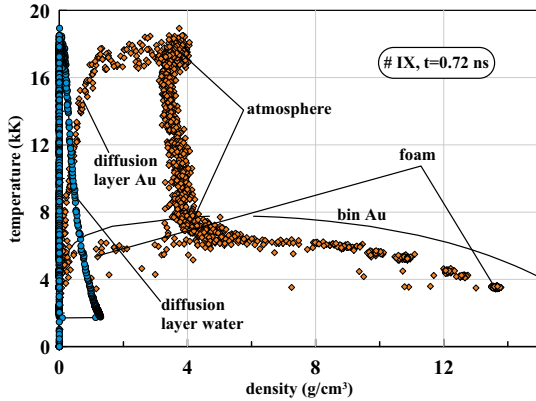


Fig. 11. Calculated profiles of density $\rho(x)$ and temperature $T(x)$ are plotted as a parametric function $T(\rho, t = 0.72)$ on a phase diagram of gold. The orange rhombuses correspond to gold, the blue circles correspond to water.

water and foam as it is shown in Fig. 10. Deceleration of the contact at the time $t = 0.72$ ns shown is $g_{ff} \approx 1.4 \cdot 10^{14}$ cm/s². When we say “atmosphere” we mean that the “free fall” deceleration $g_{ff}(t)$ changes in time more slow than the current acoustic time scale $t_s = h_{atm}/(c_s|_{atm})$.

Gold in atmosphere is in the supercritical states as it is shown in Fig. 11. Thermal effects in such states overcome the cohesive properties of interatomic attractions. As a result, the surface tension at the interface between supercritical gold and supercritical water disappears, which enhances strongly their mixing via inter-diffusion.

The maximum pressure and temperature in the atmosphere are 2 GPa and 18 kK, see Fig. 9. Thickness of atmosphere h_{atm} is 0.5 μm according to Figs. 9 and 10. In hydrostatic equilibrium, we have $h_{atm} = k_B T_{atm}/m_{Au} g_{ff}$, where k_B is Boltzmann constant and m_{Au} is mass of gold atom. Taking $T = 15$ kK as an average temperature in the atmosphere and $g_{ff} \approx 1.4 \cdot 10^{14}$ cm/s², we obtain $h_{atm} = 0.45$ μm. As the deceleration $g_{ff}(t)$ decreases with time, the height of atmosphere increases and a quasi-hydrostatic approximation loses its applicability.

Estimate of speed of sound in atmosphere based on gaseous approximation is $c_{s|atm} = \sqrt{(5/3)k_B T/m_{Au}} \approx 1$ km/s for $T = 15$ kK. Then, the current acoustic time scale is $t_s = 0.5$ ns.

Atmosphere is convectively unstable because its hotter layers in an effective gravity field are located below the colder layers in the non-inertial frame connected with a contact. But it seems that there is not enough time to develop convection because the temporal interval of deceleration is limited to few nanoseconds and there are diffusion and viscosity dumping this development. Even stronger Rayleigh-Taylor instability at the contact is suppressed in presence of diffusion. The Rayleigh-Taylor instability is stronger than the convective instability because its increment is larger since the density contrast at the contact

is larger than the entropy contrast inside the atmosphere.

We do not see any indications of convection development in MD simulation #VIII listed in Table 1. The simulation box in #VIII has the large lateral size in order to trace development of the multi-dimensional instability. But the Rayleigh-Taylor instability develops very weakly in the conditions corresponding to simulations # VIII and # IX.

Velocity of the contact zone is ≈ 800 m/s at the time $t = 0.72$ ns presented in Figs. 9– 11. Expansion velocity of the diffusion zone (from one edge to another one, concentrations change from 0% to 100%) thanks to difference of hydrodynamic velocities at the edges is 100 m/s at this time. Due to diffusion, the expansion velocity of a gold/water mixture relative to material is $(d/dt)2\sqrt{D}t = 12$ m/s for $t = 0.72$ ns and diffusion coefficient $D = 0.001$ cm²/s.

4.3. Times around 10 ns

Qualitative changes in structure of flow take place during the time interval between $t \sim 1$ ns and $t \sim 10$ ns. Structure described above in Figs. 9–11 corresponding to the stage $t \sim 1$ ns was supported thanks to momentum and kinetic energy of atmosphere and foam, which was directed to the water side, see Fig. 10. Water resists to expansion of gold, because of this resistance the momentum accumulated gradually in the gold atmosphere and foam is transferred to water. Therefore, it is not surprising that at some time all momenta of gold directed to water are exhausted.

After that, pressure in the contact zone is supported by gas and saturation pressure of hot gold. Momentum transfer and resistance of water maintain the “free fall” or quasi-gravity like (thanks to the Einstein principle of equivalence of gravitational and inertial mass) deceleration g_{ff} of a gold/water contact. In turn, the deceleration g_{ff} leads to creation of the atmospheric like quasi-hydrostatic layer of gold decelerated by the contact.

Deceleration leads to stopping of the contact. Velocity of the contact decreases to zero value and after that changes sign — the slow back motion of gold begins. At the same stage, the deceleration g_{ff} drops down to small values. Thus, thickness of the corresponding “atmosphere” and acoustic time scale for sound to pass atmosphere become larger than spatial and temporal scales related to current motion. Then, the atmosphere disappears as a significant part of the structure.

Returning to the initial stages, we have to mention that the opposite directed momenta in gold appear after laser heating and creation of the HAZ in gold. The positive momentum, directed to the bulk of gold, is taken away by the shock propagating in gold. The negative momentum is initially accumulated in the near contact layer of gold expanding to water, and then it transits to the shock in water and the compressed layer of water due to resistance of water.

Figs. 12–15 present the situation corresponding to the transient stage. This is the transient from the momentum transfer stage to the stage when pressure at the contact zone is supported by the gas and vapor pressure of slowly cooling gold. Such cooling is slow because thermal conductivity in gaseous and foam gold is much less than in condensed phase.

Pressure of gold near the contact drops down by approximately ten times during the times from 0.72 ns to 9.2 ns, compare Figs. 9 and 12. Pressure gradient in a gold layer near the contact decreases by $\approx 10^2$ times from 2 GPa per 0.7 μm to 800 bar per 2.5 μm. Density decreases from 4 g/cm³ to approximately 1 g/cm³, compare Figs. 9–11 and 12–15. Geometrical thickness of the near contact gold layer increases approximately by 3.5 times.

Decrease of deceleration g_{ff} (while temperatures decreases much more slowly and remains high at the times $t \sim 10$ ns) causes an increase of atmosphere height h_{atm} . This process looks like a back flow or outflow of gaseous gold from the contact. Velocity of gold turns back from the direction oriented to water side. To quantify the scale of this re-orientation, let's compare Figs. 10 and 13.

The outflow of gold achieves significant velocities exceeding local

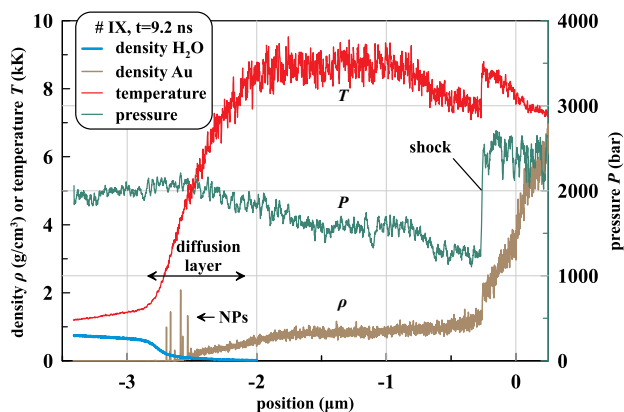


Fig. 12. Temperature, pressure and density profiles from MD simulation. Small amount of atomic gold falls below the condensation curve and begin to condense forming nanoparticles of gold inside the diffusion layer. The brown vertical straight lines near the edge of the diffusion layer point out the gold nanoparticles (NPs). Weak jump at the pressure and density profiles corresponds to a shock separating back flow of gold and the rest of the motionless gold target. Direction of motion in the back flow is shown in Fig. 13.

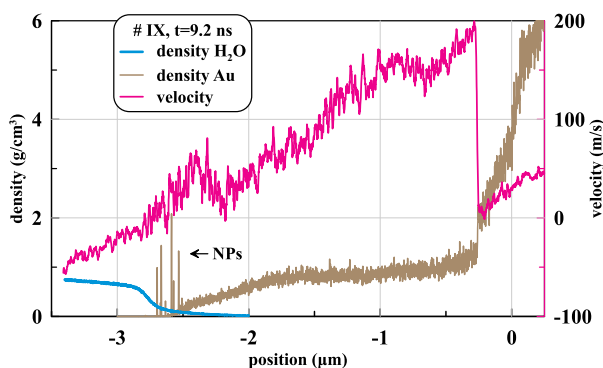


Fig. 13. Velocity and density profiles from MD simulation. Comparison with profiles in Fig. 10 demonstrates that motion of gold changes its direction from that oriented to water to the opposite one, but the velocity of diffusion layer drops down to zero due to stopping of the contact zone. A weak shock appears in the place where gaseous gold moving to the right meets approximately motionless but dense liquid gold.

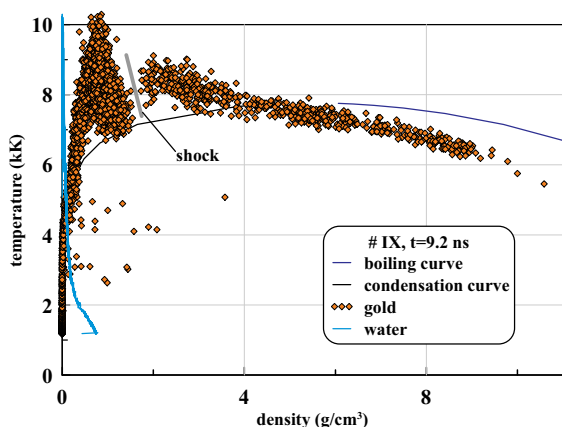


Fig. 14. Profile $T(\rho, t = 9.2 \text{ ns})$ at a phase diagram of gold. The orange rhombuses correspond to gold, the blue circles correspond to water. The line “shock” separates the rest of a target and the gaseous cloud moving in direction to the rest of target. Part of gold cooled to $T = 2\text{--}4 \text{ kK}$ and located below the condensation curve form nanoparticles inside the diffusion layer shown in Figs. 12 and 13.

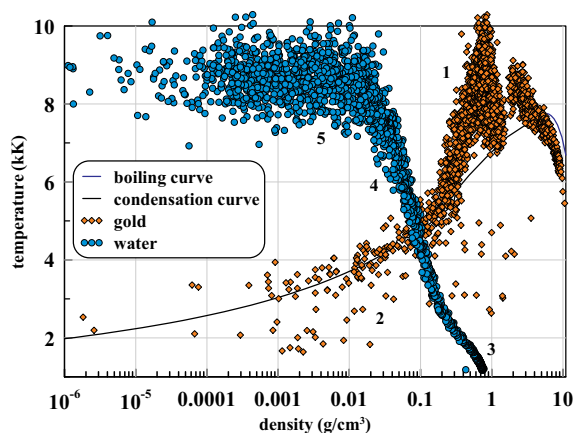


Fig. 15. The same as in Fig. 14 but using logarithm of density to see small details. The orange rhombuses correspond to gold, the blue circles correspond to water. The numerals are: 1 is gaseous gold located between the contact and the shock; 2 is gold in the diffusion layer below the condensation curve, part of this gold condenses into nanoparticles; 3 is water outside the diffusion zone; 4 is water diffused into gold; 5 is negligible amount of water deep inside gold — number of circles isn't proportional to mass of water, mass of water presented by this group of the circles is infinitesimally small.

speed of sound. Thus, a weak shock with position marked in Fig. 12 forms in the place where the outflow impacts dense molten motionless gold belonging to the boiling curve of binodal curve, see also Fig. 14. According to Fig. 13, the velocity jump at this shock is near 200 m/s. An estimate of sound speed as $c_s = \sqrt{(5/3)k_B T/m_{Au}}$ gives 730 m/s for temperature of $T = 7.5 \text{ kK}$ in gaseous gold near the left side of the jump, see Fig. 12. Another estimate based on the slope of the condensation curve $c_s = \sqrt{\Delta p/\Delta \rho}$ gives 390 m/s, here the differences Δp and $\Delta \rho$ are taken along the condensation curve. Speed of sound from EAM interatomic potential of gold used in MD simulations # VIII and # IX should be less than 200 m/s in the conditions corresponding to the state near the jump.

Expansion of gold, decreases of its density and temperature mainly due to diffusive mixing with much colder water lead to condensation of atomic gold in clusters and nanoparticles. Due to cooling, the gaseous gold intersects the condensation curve shown in Figs. 14 and 15. Nanoparticles marked by “NPs” are seen at the density profile of gold in Figs. 12–13. Those NPs begin to appear after $t \sim 1 \text{ ns}$ and then NPs number and their sizes grow with time.

Open question remains about total number of nanoparticles produced by a laser pulse. They are located in a cloud between the contact and the jump in Figs. 12–13. Indeed, there is significant quantity of gaseous gold above the condensation curve in Figs. 14 and 15, but it is unclear, how much of them will have time to condense before they collide with continuous gold corresponding to the rest of a gold target. Longer simulations should be performed to address this problem. Nevertheless, it is obvious that the nanoparticles mixed with water have no chance to return to the rest of gold target.

5. Heating of water and bubble formation

5.1. Equation of state for water and shock adiabat

We have probed three equation of states (EoS) for water. They are the van der Waals EoS, the Tait EoS, and a semi-analytical EoS developed by Nigmatulin and Bolotnova [42]. Such EoS are required to describe (a) Hugoniot adiabetic curve, (b) binodal curve of water, (c) one-phase adiabetic curves passing from the Hugoniot adiabat to binodal, and (d) two-phase adiabats presenting prolongations of the one-phase adiabats through intersection with binodal into two-phase vapor-liquid mixture. Thus, a wide range of phase states excluding solid should be

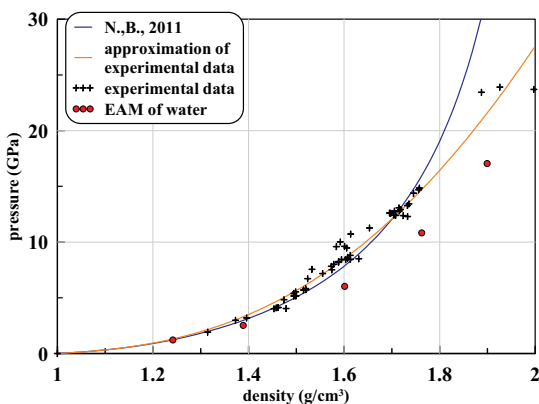


Fig. 16. Comparison of EoS [42] with experimental data on shock compression from Refs. [17, 18]. We also compare with experiment the Hugoniot adiabat curve following from the EAM potential for water used in simulations # VIII, #IX. The abbreviation N.,B., 2011 relates to the paper [42]. Semi-analytic approximation of experimental data is taken from Refs. [10, 11]. It is valid from infinitesimal compressions and up to 120 GPa — the highest measured pressures.

covered. The standard van der Waals EoS is relevant around a two-phase region. But it has rather large excluded volume and cannot be applied for approach to the Hugoniot curve with significant compressions of liquid water from the normal conditions. The Tait EoS is better near Hugoniot but it is difficult to connect the Hugoniot and binodal curves using it. The EoS [42] is valid in the wide region of the water phase diagram from the Hugoniot to binodal.

Shock adiabat of water starting from the normal state according to measurements [17, 18] is shown in Fig. 16 together with the shock Hugoniot used in our calculations. We see that the EoS [42] can be used for compressions below 17 GPa and it has a right speed of sound in the acoustic limit. The EAM interatomic potential for “mechanical” water developed by Zhakhovsky [43] gives a correct approximation of the experimental Hugoniot in a wide range of pressures up to the Megabar region.

The range of pressures up to 17–18 GPa, where the EoS [42] is applicable, is enough for our study of gold ablation into water. Indeed, the acoustic impedance of water is low relative to the impedance of gold. Therefore, even the most powerful laser pulse with an ultrashort duration corresponding to simulations # VIII and # IX from Table 1 produces moderate compressions in water, see Fig. 7. Pressures in gold are above Megabar while in water they remain below 20 GPa.

To address the important problem of formation of a bubble filled with water vapor, we have to know the thermal history of the water layers adjoining to the contact with gold. There are two sources of heating of water: first is dissipation of kinetic energy thanks to friction inside a shock-wave front, second is conductive heating of water from the hot gold. The Hugoniot curves are shown at the density-temperature plane in Fig. 17. We see that the shock heating is satisfactorily described. Comparison with the experimental temperatures is also given in Ref. [42], where it shows that the EoS [42] correctly presents shock heating up to a few kK.

5.2. Transition from strongly supercritical states to huge rarefactions of water

Let's consider first the dissipation in shock ignoring the thermal conduction. Then water cools down along an adiabat curve during expansion without thermal exchange with surrounding material. An example of this curve is shown in Fig. 18. The adiabat curve is separated to two parts: one (s1) is along the condensed phases, while another (s2) is in vapor-liquid mixture.

The adiabat curve shown in Fig. 18 starts from a point on the

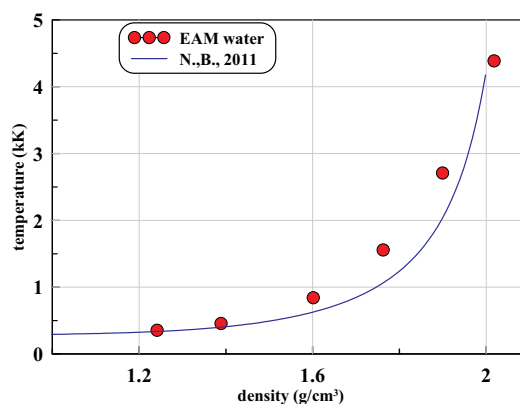


Fig. 17. Heating of water by shock is shown.

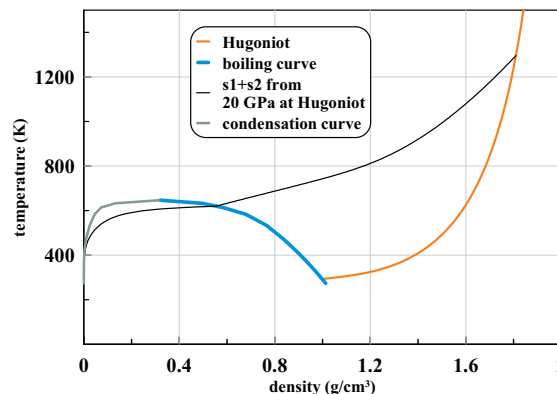


Fig. 18. Expansion of water from a shock compressed state down to binodal where water changes from the condensed phase to gaseous phase. Expansion is accompanied with adiabatic cooling of water. The adiabat curve consists from two parts s1 and s2. The first part s1 corresponds to the one-phase interval. It covers the way from the initial point at the Hugoniot adiabat curve to the intersection point between the adiabat curve and binodal. The second part s2 covers expansion inside the two-phase region. Calculations are made using EoS [42]. The initial pressure was 20 GPa.

Hugoniot for water. Initial pressure is 20 GPa in this point, which is the highest possible pressure in water for gold ablation in water. Nevertheless, the adiabat curve crosses the binodal curve at its right branch corresponding to the boiling curve below the critical point. In such case, the entropy is less than entropy of adiabatic expansion passing the binodal through the critical point.

This limits expansion of water when pressure drops down to 0.1 bar level, see Fig. 19. The adiabat curves starting from Hugoniot adiabat curve at 20, 10, 5, and 3 GPa are shown in Fig. 20. Expansion of water along the strongest adiabat curve beginning from 20 GPa and finishing at 0.1 bar gives increase in volume by 6000 times relative to the volume of water at normal conditions before the laser pulse. While for adiabat curve starting from the Hugoniot at 3 GPa, the expansion degree at $p = 0.1$ bar is only ≈ 10 , see Fig. 20. This means that the water bubble is filled with water vapor corresponding to different entropy values. The coldest layers produce the outer shells of bubble.

Cooling history and temperature decrease are shown in Fig. 21. Temperature decreases approximately twice during three times expansion along the one-phase interval s1 of the adiabat curve. After that, the temperature decreases again twice in the two-phase interval s2, but now expansion degree is ≈ 2500 times.

6. Conclusion

Ablation of gold in water is considered in different regimes of laser

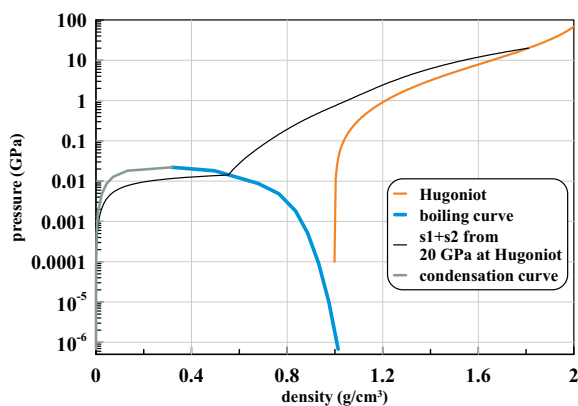


Fig. 19. The adiabatic curve $s_1 + s_2$ from Fig. 18 is shown at the density-pressure phase diagram. Pressure in a water layer drops to the atmospheric pressure.

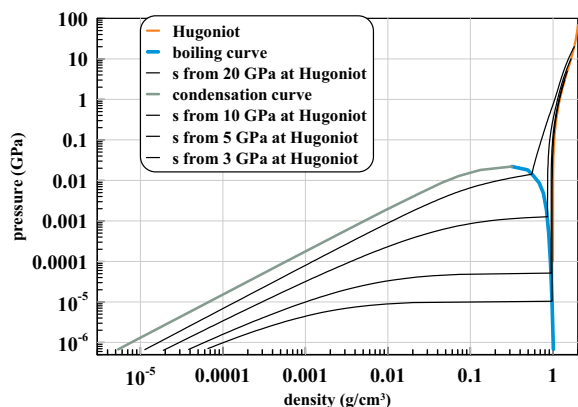


Fig. 20. This plot taken from Fig. 19 but now in double logarithmic scales in order to see how large is expansion degree at pressures about 1 bar and below.

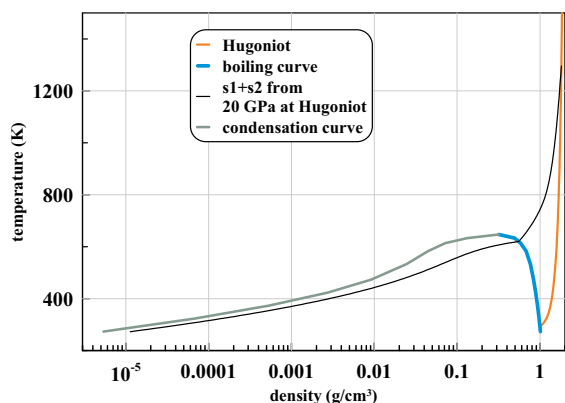


Fig. 21. Temperature decreases with expansion. The shock heated water is at $T \approx 1.3$ kK. During expansion by 6000 times to pressure of 0.1 bar the temperature drops down to $T \approx 320$ K.

heating, by varying the absorbed energy and pulse duration. Structure of ablation flow and its transformation are analyzed. It is shown that strong pulse drives gold into the supercritical states, and hot water nearby the contact with gold exists in its supercritical states for a long time due to its lower critical parameters. Evolution of pressure and temperature of water and gold during their motion is simulated. Hot compressed water and gold actively interpenetrate by fast diffusion, which results in rather thick mixed layer.

Because the temperature decreases in this layer, gold vapor crosses

the condensation curve which leads to formation of clusters and nanoparticles. Those nanoparticles are surrounded by water, thus they cannot stick back to bulk target remnants and remain in water during its expansion.

Acknowledgements

Authors (YVP, VAK, NAI) acknowledge support from the order of the state (0033-2019-0007).

Appendix A

The iteration scheme in Lagrangian variables is employed in hydrodynamic simulations presented in the main text. A cycle of iterations is executed during a time step. The cycle consists from two stages: hydrodynamic and thermodynamic. The hydrodynamic stage is executed according to a conservative scheme described in Ref. [44]. The thermodynamic stage is executed separately for electron and ion subsystems. The electron-ion separation by the scheme [44] was implemented in our group: a separation of the thermal equations was proposed in Ref. [20] (the two-temperature state in a motionless substance). The hydrodynamic version of the equations [20] is utilized in our code 2T-HD, which was previously used in Refs. [22, 29, 30, 45–48].

Articles [45, 46] describe the 2T-HD and MD codes, their combination and comparisons of the simulation results with experiments. The procedure for generating initial data for MD using the 2T-HD code is described in Refs. [47, 49]. In addition, those works provide comparisons with MD simulation data from other authors on the same targets.

To check the design schemes and the physical models used in the 2T-HD and MD codes, comparisons with the high accuracy experimental measurements of the processes of formation of the shock wave and its propagation over the film were made in the works [29, 30]. The breakthrough time of the film by the shock wave and the velocity of the substance behind the shock wave were measured with high accuracy in experiments [29, 30] and compared with simulations [29, 30].

Prediction and comparison with experiment of data on the formation of a porous surface layer was another test of numerical methods used in our MD approach [50]. A large number of calculations using 2T-HD and MD-MC codes was performed to describe experimental solitary structures (bulging of a film in the form of a dome) on thin films [51]. The bulging is produced by an action of a tightly focused ultrashort laser pulse.

In the 2T-HD code, an electron energy equation is solved taking from the hydrodynamic stage the distributions of density, temperatures, and velocity along Lagrangian cells. The sweep method [44] (implicit scheme) is used to solve electron energy equation with thermal conduction.

We neglect in metals an ion thermal conduction because it is small relative to an electron thermal conduction. Then an ion energy equation becomes a simple differential equation. Energy exchange between electron and ion subsystems is calculated in every cell taking electron and ion temperatures from a previous iteration. The procedure keeps conservation character of the scheme.

Using densities from the hydrodynamic stage and temperatures (electron and ion) from the thermodynamic stage, we calculate electron and ion pressures. A sum of these pressures is total pressure. Distribution of total pressures along the Lagrangian cells is employed in the hydrodynamic stage of the next iteration. Convergence of iterations is controlled. The control defines length of the step in time — if convergence is fast then the time step is enlarged.

For ion subsystem, we use tables of a wide-range equation of state [14–18]. Thermodynamic electron additions, coefficients of thermal conduction and electron-ion coupling parameter are taken from papers [21, 52, 53], see also Refs. [22, 48] where two-temperature physics was presented.

This hydrodynamic approach was used in our previous papers devoted to physics of laser ablation [11, 31]. System of equations of two-temperature hydrodynamics is given in Ref. [11].

The code similar to the code used in paper [11] was employed for molecular dynamics simulations presented above. Only absorbed energy in the simulations shown in the present paper was higher, see Table 1 in Section 2. Simulation # IX in Table 1 has cross-section $y \times z = 9.8 \times 9.8 \text{ nm} \times \text{nm}$. Initial length of a water-gold system was $4 \mu\text{m}$. Initial position of a contact boundary between gold and water was $x = 0$. Length of a computational box along the axis x is $8 \mu\text{m}$. Thus, we use narrow and very long box. This is necessary to follow the late time evolution of a system.

Initial number of atoms of gold was 11,279,232. We cut deep layers of gold after cavitation and formation of foam. This speeds up simulation. The same procedure was used in Ref. [11]. It doesn't influence evolution of the layers near the contact. To describe this evolution is the main goal of the paper. 1,780,214 atoms of gold remain after cutting.

Initially, it was 6,372,951 particles of water. We use the same method of cutting of a part of a water layer as it is described in details in Ref. [11]. After this, cutting the water layer is located between a contact and a moving piston. Trajectory of the piston was defined in the preliminary simulations, see Ref. [11]. There are 1,597,495 particles in water after activation of the piston.

EAM potential for gold was developed in paper [54]. The used potential for water is described in Ref. [43].

References

- [1] D. Zhang, B. Gökce, S. Barcikowski, Laser synthesis and processing of colloids: fundamentals and applications, *Chem. Rev.* 117 (5) (2017) 3990–4103, <https://doi.org/10.1021/acs.chemrev.6b00468>.
- [2] J. Xiao, P. Liu, C. Wang, G. Yang, External field-assisted laser ablation in liquid: an efficient strategy for nanocrystal synthesis and nanostructure assembly, *Prog. Mater. Sci.* 87 (2017) 140–220, <https://doi.org/10.1016/j.pmatsci.2017.02.004>.
- [3] S.V. Starinskiy, Y.G. Shukhov, A.V. Bulgakov, Laser-induced damage thresholds of gold, silver and their alloys in air and water, *Appl. Surf. Sci.* 396 (2017) 1765–1774, <https://doi.org/10.1016/j.apsusc.2016.11.221>.
- [4] J. Lam, J. Lombard, C. Dujardin, G. Ledoux, S. Merabia, D. Amans, Dynamical study of bubble expansion following laser ablation in liquids, *Appl. Phys. Lett.* 108 (7) (2016) 074104, <https://doi.org/10.1063/1.4942389>.
- [5] M.E. Povarnitsyn, T.E. Itina, P.R. Levashov, K.V. Khishchenko, Mechanisms of nanoparticle formation by ultra-short laser ablation of metals in liquid environment, *Phys. Chem. Chem. Phys.* 15 (2013) 3108–3114, <https://doi.org/10.1039/C2CP42650A>.
- [6] M.E. Povarnitsyn, T. Itina, Hydrodynamic modeling of femtosecond laser ablation of metallic targets in vacuum and in liquid, *Appl. Phys. A* 117 (1) (2014) 175–178, <https://doi.org/10.1007/s00339-014-8319-1>.
- [7] M.E. Povarnitsyn, V.B. Fokin, L.V. Levashov, Microscopic and macroscopic modeling of femtosecond laser ablation of metals, *Appl. Surf. Sci.* 357 (2015) 1150–1156, <https://doi.org/10.1016/j.apsusc.2015.09.131>.
- [8] C.-Y. Shih, M.V. Shugaev, C. Wu, L.V. Zhigilei, Generation of subsurface voids, incubation effect, and formation of nanoparticles in short pulse laser interactions with bulk metal targets in liquid: molecular dynamics study, *J. Phys. Chem. C* 121 (2017) 16549–16567.
- [9] C.-Y. Shih, R. Streubel, J. Heberle, A. Letzel, M.V. Shugaev, C. Wu, M. Schmidt, B. Gokce, S. Barcikowski, L.V. Zhigilei, Two mechanisms of nanoparticle generation in picosecond laser ablation in liquids: the origin of the bimodal size distribution, *Nanoscale* 10 (2018) 6900–6910, <https://doi.org/10.1039/C7NR08614H>.
- [10] N. Inogamov, V. Zhakhovskiy, V. Khokhlov, Laser Ablation of Gold into Water: Near Critical Point Phenomena and Hydrodynamic Instability, [arXiv:1803.07343v1](https://arxiv.org/abs/1803.07343v1), (2018) [physics.comp-ph].
- [11] N.A. Inogamov, V.V. Zhakhovskii, V.A. Khokhlov, Dynamics of gold ablation into water, *JETP* 127 (1) (2018) 79–106, <https://doi.org/10.1134/S1063776118070075>.
- [12] D.S. Ivanov, V.P. Lipp, A. Blumenstein, F. Kleinwort, V.P. Veiko, E. Yakovlev, V. Roddatis, M.E. Garcia, B. Rethfeld, J. Ihlemann, P. Simon, Experimental and theoretical investigation of periodic nanostructuring of Au with ultrashort UV laser pulses near the damage threshold, *Phys. Rev. Appl.* 4 (2015) 064006, <https://doi.org/10.1103/PhysRevApplied.4.064006> <https://link.aps.org/doi/10.1103/PhysRevApplied.4.064006>.
- [13] D.S. Ivanov, A. Blumenstein, J. Ihlemann, P. Simon, M.E. Garcia, B. Rethfeld, Molecular dynamics modeling of periodic nanostructuring of metals with a short UV laser pulse under spatial confinement by a water layer, *Appl. Phys. A* 123 (2017) 744, <https://doi.org/10.1007/s00339-017-1372-9>.
- [14] A.V. Bushman, V.E. Fortov, G.I. Kanel, A.L. Ni, *Intense Dynamic Loading of Condensed Matter*, Taylor & Francis Translation, London, 1993.
- [15] K.V. Khishchenko, S.I. Tkachenko, P.R. Levashov, I.V. Lomonosov, V.S. Vorob'ev, Metastable states of liquid tungsten under subsecond wire explosion, *Intern. J. Thermophys.* 23 (5) (2002) 1359–1367, <https://doi.org/10.1023/A:1019821126883>.
- [16] I. Lomonosov, Multi-phase equation of state for aluminum, *Laser Part. Beams* 25 (4) (2007) 567–584, <https://doi.org/10.1017/S0263034607000687>.
- [17] <http://teos.ficp.ac.ru/rusbank/>, <http://teos.ficp.ac.ru/rusbank/>.
- [18] <http://www.ihed.ras.ru/rusbank/>, <http://www.ihed.ras.ru/rusbank/>.
- [19] L.V. Zhigilei, Z. Lin, D.S. Ivanov, Atomistic modeling of short pulse laser ablation of metals: connections between melting, spallation, and phase explosion, *J. Phys. Chem. C* 113 (27) (2009) 11892–11906, <https://doi.org/10.1021/jp902294m>.
- [20] S.I. Anisimov, B.L. Kapeliovich, T.L. Perel'man, Electron emission from metal surfaces exposed to ultrashort laser pulses, *Sov. Phys. JETP* 39 (2) (1974) 375–377 <http://www.jetp.ac.ru/cgi-bin/r/index/e/39/2/p375?a=list>.
- [21] Y.V. Petrov, N.A. Inogamov, K.P. Migdal, Thermal conductivity and the electron-ion heat transfer coefficient in condensed media with a strongly excited electron subsystem, *JETP Lett.* 97 (1) (2013) 20–27, <https://doi.org/10.1134/S0021364013010098>.
- [22] K.P. Migdal, Y.V. Petrov, N.A. Inogamov, Kinetic coefficients for d-band metals in two-temperature states created by femtosecond laser irradiation, *Proc. SPIE* 9065 (2013), <https://doi.org/10.1117/12.2053172> 9065 – 9065 - 20.
- [23] N.A. Inogamov, V.V. Zhakhovskiy, S.I. Ashtikov, V.A. Khokhlov, V.V. Shepelev, P.S. Komarov, A.V. Ovchinnikov, D.S. Sitnikov, Y.V. Petrov, M.B. Agranat, S.I. Anisimov, V.E. Fortov, Laser acoustic probing of two-temperature zone created by femtosecond pulse, *Contrib. Plasma Phys.* 51 (4) (2011) 367–374, <https://doi.org/10.1002/ctpp.201010111>.
- [24] N.A. Inogamov, V.V. Zhakhovskiy, Y.V. Petrov, V.A. Khokhlov, S.I. Ashtikov, K.P. Migdal, D.K. Il'nitskiy, Y.N. Emirov, K.V. Khishchenko, P.S. Komarov, V.V. Shepelev, M.B. Agranat, S.I. Anisimov, I.I. Oleynik, V.E. Fortov, Ultrashort laser-matter interaction at moderate intensities: two-temperature relaxation, foaming of stretched melt, and freezing of evolving nanostructures, *Proc. SPIE* 9065 (2013), <https://doi.org/10.1117/12.2053166> 9065 – 9065 - 14.
- [25] S.I. Ashtikov, P.S. Komarov, V.V. Zhakhovskiy, Y.V. Petrov, V.A. Khokhlov, A.A. Yurkevich, D.K. Il'nitskiy, N.A. Inogamov, M.B. Agranat, Ablation of gold irradiated by femtosecond laser pulse: experiment and modeling, *J. Phys. Conf. Ser.* 774 (1) (2016) 012097 <http://stacks.iop.org/1742-6596/774/i=1/a=012097>.
- [26] K. Eidmann, J.M. ter Vehn, T. Schlegel, S. Hueller, Hydrodynamic simulation of subpicosecond laser interaction with solid-density matter, *Phys. Rev. E* 62 (2000) 1202–1214.
- [27] Z. Chen, M. Mo, L. Souillard, V. Recoules, P. Hering, Y.Y. Tsui, S.H. Glenzer, A. Ng, Interatomic potential in the nonequilibrium warm dense matter regime, *Phys. Rev. Lett.* 121 (7) (2018), <https://doi.org/10.1103/PhysRevLett.121.075002>.
- [28] Y.V. Petrov, N.A. Inogamov, Elimination of the Mott interband s-d enhancement of the electrical resistance of nickel and platinum owing to the excitation of electrons by femtosecond laser pulses, *JETP Lett.* 98 (5) (2013) 278–284, <https://doi.org/10.1134/S0021364013180094>.
- [29] N.A. Inogamov, V.V. Zhakhovskii, V.A. Khokhlov, V.V. Shepelev, Superelasticity and the propagation of shock waves in crystals, *JETP Lett.* 93 (4) (2011) 226–232, <https://doi.org/10.1134/S0021364011040096>.
- [30] B.J. Demaske, V.V. Zhakhovskiy, N.A. Inogamov, I.I. Oleynik, Ultrashort shock waves in nickel induced by femtosecond laser pulses, *Phys. Rev. B* 87 (2013) 054109, <https://doi.org/10.1103/PhysRevB.87.054109>.
- [31] N. Inogamov, V. Zhakhovskii, S. Ashtikov, V. Khokhlov, Y. Petrov, P. Komarov, M. Agranat, S. Anisimov, K. Nishihara, Two-temperature relaxation and melting after absorption of femtosecond laser pulse, *Appl. Surf. Sci.* 255 (24) (2009) 9712–9716, <https://doi.org/10.1016/j.apsusc.2009.04.139> Proceedings of the Sixth International Conference on Photo-Excited Processes and Applications (6-ICPEPA).
- [32] N.A. Inogamov, V.V. Zhakhovskiy, S.I. Ashtikov, Y.N. Emirov, A.Y. Faenov, N.A. Pikuz, M. Ishino, M. Kando, N. Hasegawa, M. Nishikino, T. Kawachi, M.B. Agranat, A.V. Andriash, S.E. Kuratov, I.I. Oleynik, Surface nano-structuring produced by spallation of metal irradiated by an ultrashort laser pulse, *J. Phys. Conf. Ser.* 500 (11) (2014) 112070, <https://doi.org/10.1088/1742-6596/500/11/112070>.
- [33] N. Inogamov, V. Zhakhovskiy, V. Khokhlov, S. Ashtikov, Y. Emirov, K. Khichshenko, A. Faenov, T. Pikuz, M. Ishino, M. Kando, N. Hasegawa, M. Nishikino, P. Komarov, B. Demaske, M. Agranat, S. Anisimov, T. Kawachi, I. Oleynik, Ultrafast lasers and solids in highly excited states: results of hydrodynamics and molecular dynamics simulations, *J. Phys. Conf. Ser.* 510 (2014) 012041, <https://doi.org/10.1088/1742-6596/510/1/012041>.
- [34] S.I. Ashtikov, P.S. Komarov, A.V. Ovchinnikov, E.V. Struleva, V.V. Zhakhovskii, N.A. Inogamov, M.B. Agranat, Ablation and nanostructuring of metals by femtosecond laser pulses, *Quant. Electron.* 44 (6) (2014) 535–539, <https://doi.org/10.1070/QE2014v04n06ABEH015448>.
- [35] A.N. Volkov, L.V. Zhigilei, Hydrodynamic multi-phase model for simulation of laser-induced non-equilibrium phase transformations, *J. Phys. Conf. Ser.* 59 (1) (2007) 640.
- [36] W.-L. Chan, R.S. Averback, D.G. Cahill, A. Lagoutchev, Dynamics of femtosecond laser-induced melting of silver, *Phys. Rev. B* 78 (2008) 214107.
- [37] D.S. Ivanov, Z. Lin, B. Rethfeld, G.M. O'Connor, T.J. Glynn, L.V. Zhigilei, Nanocrystalline structure of nanobump generated by localized photoexcitation of metal film, *J. Appl. Phys.* 107 (1) (2010) 013519, <https://doi.org/10.1063/1.3276161>.
- [38] D.S. Ivanov, A.I. Kuznetsov, V.P. Lipp, B. Rethfeld, B.N. Chichkov, M.E. Garcia,

- W. Schulz, Short laser pulse nanostructuring of metals: direct comparison of molecular dynamics modeling and experiment, *Appl. Phys. A* 111 (3) (2013) 675–687, <https://doi.org/10.1007/s00339-013-7656-9>.
- [39] N.A. Inogamov, V.V. Zhakhovskiy, K.P. Migdal, Laser-induced spalling of thin metal film from silica substrate followed by inflation of microbump, *Appl. Phys. A* 122 (4) (2016) 432, <https://doi.org/10.1007/s00339-016-9942-9>.
- [40] N.A. Inogamov, V.V. Zhakhovskiy, V.A. Khokhlov, Y.V. Petrov, K.P. Migdal, Solitary nanostructures produced by ultrashort laser pulse, *Nanoscale Res. Lett.* 11 (1) (2016) 177, <https://doi.org/10.1186/s11671-016-1381-1>.
- [41] S.I. Anisimov, V.V. Zhakhovskiy, N.A. Inogamov, S.A. Murzov, V.A. Khokhlov, Formation and crystallisation of a liquid jet in a film exposed to a tightly focused laser beam, *Quant. Electron.* 47 (6) (2017) 509–521, <https://doi.org/10.1070/QEL16381>.
- [42] R.I. Nigmatulin, R.K. Bolotnova, Wide-range equation of state for water and steam: simplified version, *High Temp.* 49 (2) (2011) 303–306, <https://doi.org/10.1134/S0018151X11020106>.
- [43] EAM-type potential for “mechanical” water, www.researchgate.net/project/Development-of-interatomic-EAM-potentials.
- [44] A.A. Samarskii, *The Theory of Difference Schemes*, CRC Press, 2001.
- [45] M.B. Agranat, S.I. Anisimov, S.I. Ashitkov, V.V. Zhakhovskii, N.A. Inogamov, P.S. Komarov, A.V. Ovchinnikov, V.E. Fortov, V.A. Khokhlov, V.V. Shepelev, Strength properties of an aluminum melt at extremely high tension rates under the action of femtosecond laser pulses, *JETP Lett.* 91 (9) (2010) 471–477, <https://doi.org/10.1134/S0021364010090080>.
- [46] N.A. Inogamov, V.V. Zhakhovskiy, S.I. Ashitkov, M.B. Agranat, P.S. Komarov, V.A. Khokhlov, V.V. Shepelev, Pump-probe method for measurement of thickness of molten layer produced by ultrashort laser pulse, *AIP Conference Proceedings* 1278 (1) (2010) 590–599, <https://doi.org/10.1063/1.3507151> arxiv:<https://aip.scitation.org/doi/pdf/10.1063/1.3507151> <https://aip.scitation.org/doi/abs/10.1063/1.3507151>.
- [47] B.J. Demaske, V.V. Zhakhovskiy, N.A. Inogamov, I.I. Oleynik, Molecular dynamics simulations of femtosecond laser ablation and spallation of gold, *AIP Conf. Proc.* 1278 (1) (2010) 121–130, <https://doi.org/10.1063/1.3507095> arxiv:<https://aip.scitation.org/doi/pdf/10.1063/1.3507095> <https://aip.scitation.org/doi/abs/10.1063/1.3507095>.
- [48] N.A. Inogamov, V.V. Zhakhovskiy, Y.V. Petrov, V. Khokhlov, S.I. Ashitkov, K.V. Khishchenko, K.P. Migdal, D.K. Ilitskiy, Y.N. Emirov, P.S. Komarov, V.V. Shepelev, C. Miller, I. Oleynik, M. Agranat, A. Andriyash, S. Anisimov, V. Fortov, Electron-ion relaxation, phase transitions, and surface nano-structuring produced by ultrashort laser pulses in metals, *Contrib. Plasma Phys.* 53 (10) (2013) 796–810, <https://doi.org/10.1002/ctpp.201310049> arxiv:<https://onlinelibrary.wiley.com/doi/pdf/10.1002/ctpp.201310049> <https://onlinelibrary.wiley.com/doi/abs/10.1002/ctpp.201310049>.
- [49] B.J. Demaske, V.V. Zhakhovskiy, N.A. Inogamov, I.I. Oleynik, Ablation and spallation of gold films irradiated by ultrashort laser pulses, *Phys. Rev. B* 82 (2010) 064113, <https://doi.org/10.1103/PhysRevB.82.064113> <https://link.aps.org/doi/10.1103/PhysRevB.82.064113>.
- [50] S.I. Ashitkov, N.A. Inogamov, V.V. Zhakhovskii, Y.N. Emirov, M.B. Agranat, I.I. Oleinik, S.I. Anisimov, V.E. Fortov, Formation of nanocavities in the surface layer of an aluminum target irradiated by a femtosecond laser pulse, *JETP Lett.* 95 (4) (2012) 176–181, <https://doi.org/10.1134/S0021364012040042>.
- [51] X.W. Wang, A.A. Kuchmizhak, X. Li, S. Juodkazis, O.B. Vitrik, Y.N. Kulchin, V.V. Zhakhovskiy, P.A. Danilov, A.A. Ionin, S.I. Kudryashov, A.A. Rudenko, N.A. Inogamov, Laser-induced translative hydrodynamic mass snapshots: non-invasive characterization and predictive modeling via mapping at nanoscale, *Phys. Rev. Appl.* 8 (2017) 044016, <https://doi.org/10.1103/PhysRevApplied.8.044016>.
- [52] Y.V. Petrov, K.P. Migdal, N.A. Inogamov, V.V. Zhakhovskiy, Two-temperature equation of state for aluminum and gold with electrons excited by an ultrashort laser pulse, *Appl. Phys. B* 119 (2015) 401–411.
- [53] Y.V. Petrov, K.P. Migdal, N.A. Inogamov, S.I. Anisimov, Transport processes in a metal with hot electrons excited by a laser pulse, *JETP Lett.* 104 (2016) 431–439.
- [54] V.V. Zhakhovskii, N.A. Inogamov, Y.V. Petrov, S.I. Ashitkov, K. Nishihara, Molecular dynamics simulation of femtosecond ablation and spallation with different interatomic potentials, *Appl. Surf. Sci.* 255(24) (2009) 9592–9596.